

Uncharacteristic second order martensitic transformation in metals via epitaxial stress fields

Authors: Samuel Temple Reeve¹, Karthik Guda Vishnu², and Alejandro Strachan^{2*}

Affiliations:

¹Materials Science Division, Lawrence Livermore National Laboratory,
7000 East Ave, Livermore, CA 94550

²School of Materials Engineering and Birck Nanotechnology Center, Purdue University,
West Lafayette, Indiana 47906 USA.

*Correspondence to: strachan@purdue.edu

Abstract

While most phase transformations, e.g. ferroelectric or ferromagnetic, can be first or second order depending on external applied fields, martensitic transformations in metallic alloys are nearly universally first order. We demonstrate that epitaxial stress originating from the incorporation of a tailored second phase can modify the free energy landscape that governs the phase transition and change its order from first to second. High-fidelity molecular dynamics simulations show a remarkable change in the character of the martensitic transformation in Ni-Al alloys near the critical point. We observe the continuous evolution of the transformation order parameter and scaling with power-law exponents comparable to those in similar transitions. Our theoretical work provides a foundation to recent experimental and computational results.

1. Introduction

Phase transformations are fascinating from a scientific point of view and critical for human development, from the production of early bronzes through the rise of steels [1] to today's phase change materials used in solar energy [2] and nanoelectronics [3]. In the field of materials science, ferroelectric transformations power actuators and sensors [4], [5] and enhance the performance of electronic devices [6]. Analogously, solid-to-solid martensitic transformations in metallic alloys, underlie shape memory, superelasticity, and strengthening in many high-performance steels [7], [8]. Under most conditions, phase transformations involve a discontinuous jump in properties; for example, as a liquid turns into vapor its density changes abruptly and as a ferroelectric material is cooled down across its Curie temperature, polarization develops suddenly [9]. However, in most cases, the character of the transformation can be changed from discontinuous (classified as first order) to continuous (second order) via the application of an external field conjugate with the order parameter that governs the transformation: electric and magnetic fields in ferroelectrics [10] and ferromagnetics, respectively, and pressure in the liquid-gas transition [9]. The change from first to second order is accompanied by striking effects, from the existence of universal scaling laws to a lack of hysteresis which can be harnessed in various applications such as sensors and actuators [11], [12]. While the existence of a critical point associated with a second order transformation is common to most phase changes, martensitic transformations in metallic alloys are stubbornly first order. While specific compositions can lead to near continuous behavior [13], we lack an external field to continuously tune the nature of these transformations and achieve criticality. In this letter we use theory and high-fidelity molecular dynamics (MD) simulations to show that the strain fields resulting from a tailored coherent

second phase can transform the nature of martensitic transformation in metallic alloys from first to second order.

A key characteristic of second order phase transformations is that many accompanying properties are described by scaling laws reflecting a lack of characteristic scales. More importantly, disparate systems often exhibit identical scaling exponents, indicating underlying universal behavior. For example, ferroic transitions, order-disorder transitions, superconductors, and superfluids [9] belong to the same universality class. Many systems beyond this list of classic examples also display critical behavior, from biology [14], to Mott transitions [15], liquid crystals [16], [17], and granular materials [18]. Our MD simulations on NiAl alloys confirm a dramatic change in the nature of transformation in the vicinity of the critical point, showing scaling behavior with exponents consistent with the mean field universality class. Our findings provide a theoretical foundation for both the recent experiments in Ti-based gum metals containing nanoscale variations in composition and exhibiting “higher-order” behavior including continuous stress-induced transformation [19], [20], as well as computational prediction of ultra-low stiffness [21], reduced hysteresis, and ability to tune transformation temperatures [22], [23] in Ni-Al alloys.

II. Methods and analysis

Quenched $\text{Ni}_x\text{Al}_{1-x}$ alloys display a martensitic transformation and shape memory between 60 and 65 at. % Ni [24]. Here, off-stoichiometric 63 at. % Ni – 37 at. % is the martensitic phase and B2 $\text{Ni}_{50}\text{Al}_{50}$ the non-martensitic second phase. The interatomic interactions were described with a potential developed by Farkas et al. [25], fit to experimental properties of Ni, Al, Ni_3Al , NiAl, Ni_5Al_3 , and $L1_0$ martensite. It has been shown to accurately capture a cubic to monoclinic martensitic transformation with reasonable transformation temperatures for the correct range of Ni compositions. The model and motivation of the approach are described in more detail in prior publications [21], [22], [26], [27].

All MD simulations were performed using LAMMPS[28]. All bulk and nanolaminate systems were created with 1,024,000 atoms, with 80 B2 unit cells in each direction, initially a cube measuring 23.2 nm. Regions of off-stoichiometric 63 at. % Ni were created by randomly swapping Ni on Al sites within a layer of the desired volume fraction. These systems match those from Reeve et al. [23] with additional volume fractions above 60 at. % NiAl. A timestep of 1 fs with velocity Verlet integration was used throughout, as well as Nosé-Hoover thermostat and barostat coupling constants of 0.01 ps and 0.1 ps, respectively.

All visualization and cluster analysis was performed with OVITO [29]. The polyhedral template matching (PTM) algorithm [30] implemented in OVITO was used for structural identification. For each atom, the local neighbor structure is compared to templates for common crystals (FCC, BCC, HCP, etc.) and the root mean square (RMS) error calculated. Each atom is then identified as the structure with the lowest error. For this work, atoms identified as BCC are referred to as austenite, HCP as martensite, and FCC as stacking faults. If no mapping exists to any of the chosen templates, the atom is listed as “other”. In addition, an RMS error cutoff of 0.12 was chosen, above which atoms were also considered “other”.

Martensite clusters were analyzed by deleting all austenite atoms with OVITO cluster analysis to determine number of clusters and OVITO surface mesh analysis to extract cluster surface area and volume for each system and temperature.

III. Engineering martensitic free energy landscapes into a continuous transformation

The discontinuous nature of a first order phase transition originates from the shape of the free energy landscapes underlying the transformation and their temperature dependence. Figure 1A shows the free energy as a function of lattice parameter for a model $\text{Ni}_{63}\text{Al}_{37}$ alloy obtained using MD for various temperatures. Free energy landscapes were calculated starting from the stable, unstrained state for each temperature and strained at a rate of $1 \cdot 10^9 \text{ ps}^{-1}$ in tension and compression. Because it is an isothermal process, the entropic term goes to zero and it is possible to obtain the free energy by integrating the stress and strain as:

$$dF = V(\sigma_{xx}d\epsilon_{xx} + \sigma_{yy}d\epsilon_{yy} + \sigma_{zz}d\epsilon_{zz} + \tau_{xy}d\gamma_{xy} + \tau_{xz}d\gamma_{xz} + \tau_{yz}d\gamma_{yz})$$

From the landscapes we see that at high temperatures the austenite phase (A) is stable and the martensite (M) is metastable. Both phases have approximately the same free energy at 950K and at lower temperatures the martensite phase is stable. These landscapes represent the typical behavior of first order transformations. Note that the two phases are separated by an energy barrier that must be overcome during the phase transformation (resulting in hysteresis) and that the austenite and martensite phases have distinct lattice parameters at all temperatures. Thus, the transformation involves a jump in properties. We hypothesized that a continuous change from one phase to another, without an energy barrier, could be achieved by modifying this martensitic energy landscape via a coherent second phase with a complementary landscape. Coherent integration at the nanoscale, involving defect free interfaces as shown in Fig. 1D, forces the two phases to share the same lattice parameters; consequently, one can think of the energy landscape of the composite metamaterial as the weighted sum of each component as a function of lattice parameter. Figure 1B exemplifies our approach of free energy landscape engineering (FELE) to achieve a barrier-less transformation. Building on our previous work [21]–[23], we considered phases with opposing stability: $\text{Ni}_{63}\text{Al}_{37}$ far below austenite metastability and the ordered $\text{Ni}_{50}\text{Al}_{50}$ for which the martensite is unstable down to 0 K. An analytical combination of these two landscapes, at 25 K, yields the desired landscapes (dashed line in Fig. 1B) with a flat landscape characteristic of second order systems. While subtler than the analytical combination, the actual landscapes obtained from direct simulation of a coherent nanolaminate of 65% NiAl and 35% $\text{Ni}_{63}\text{Al}_{37}$, Fig. 1C, indeed shows typical features expected in a second order phase transformation. The system continuously moves from the high-temperature austenite to the martensite phase without a barrier.

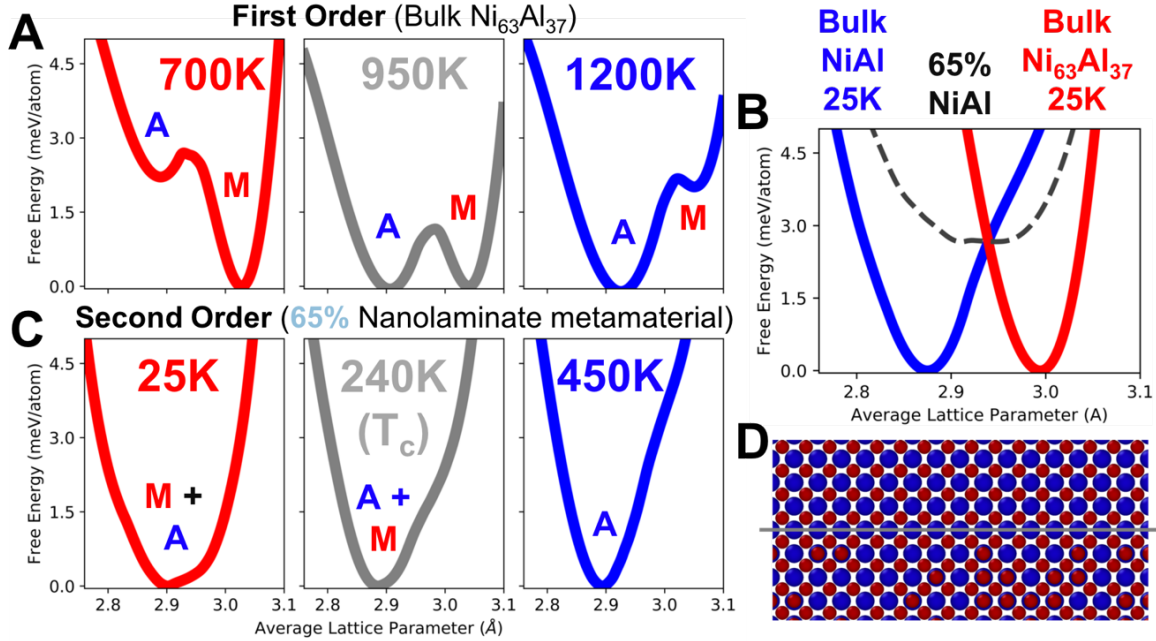


Fig. 1. Free energy landscape engineering producing the possibility of second order behavior. (A) Calculated free energy landscapes for a bulk, first order $\text{Ni}_{63}\text{Al}_{37}$ martensitic alloy, (B) analytically combined free energy landscape from separate NiAl and $\text{Ni}_{63}\text{Al}_{37}$ bulk systems at low temperature, (C) free energy landscapes for a 65 at. % NiAl nanolaminate, and (D) atomic interface between NiAl (top) and $\text{Ni}_{63}\text{Al}_{37}$ (bottom) with Al blue and Ni red.

IV. Critical martensitic transformation and scaling laws

The free energy landscape shown in Fig. 1C provides strong evidence for the second order nature of the transformation in the coherent metamaterial. To confirm this expectation and to characterize features of the transformation, we carried out explicit MD simulations of the thermal transformation. Coherent laminates with period 11.6 nm and cross-sectional areas of 23.2 nm (interface shown in Fig. 1D) were cooled from above the martensitic transformation temperature (M_s) to 25 K under isothermal-isobaric conditions (NPT) at a rate of $1 \cdot 10^{11}$ K/s and then heated above the austenite finish (A_f) temperature at the same rate. During heating and cooling, all directions and angles were left free to relax at 1 atm pressure. We characterized the nature of the thermal transformation by analyzing the thermodynamic response of the coherent metamaterial as a function of the volume fraction of the NiAl second phase and exploring possible scaling laws. In addition, a detailed local structure analysis of the atomistic trajectories was used to identify phases, revealing domain structure and size distributions characteristic of critical phenomena with marked differences from the bulk $\text{Ni}_{63}\text{Al}_{37}$ alloy.

A. Strain order parameter exponent

We define the transformation order parameter as the martensitic transformation strain along the in-plane direction for the nanolaminates; this is analogous to ferroelectric polarization and ferromagnetic magnetization. The bulk alloy shows the baseline characteristics of transformation strain as a function of temperature (shifted by M_s), see the red line in Fig. 2. This transformation shows first order characteristics, with an abrupt jump from almost entirely austenite to fully martensite during cooling. Adding up to 50 at.

% of the non-transforming NiAl phase does not change the transformation in a significant manner; we see an abrupt, but incomplete, transformation. As hypothesized from the free energy landscapes in Fig. 1C, 65 at. % NiAl and higher fractions results in distinct behavior, with a continuous increase in the order parameter. Despite the intrinsic fluctuations characteristic of relatively small systems with off-stoichiometric composition, the change from discontinuous to a continuous transformation is clear in Fig. 2. Further support of the continuous nature of the transformation is a near zero hysteresis in the transformation for all systems above 60 at. % NiAl, see Supplemental Fig. 1. Furthermore, the evolution of this order parameter for $T < T_c$ can be described with a power law, see details in Supplemental Fig. 2. The corresponding critical exponent, β , ranges between 0.45 and 0.55 for 65 at. % NiAl, consistent with other similar systems as discussed below.

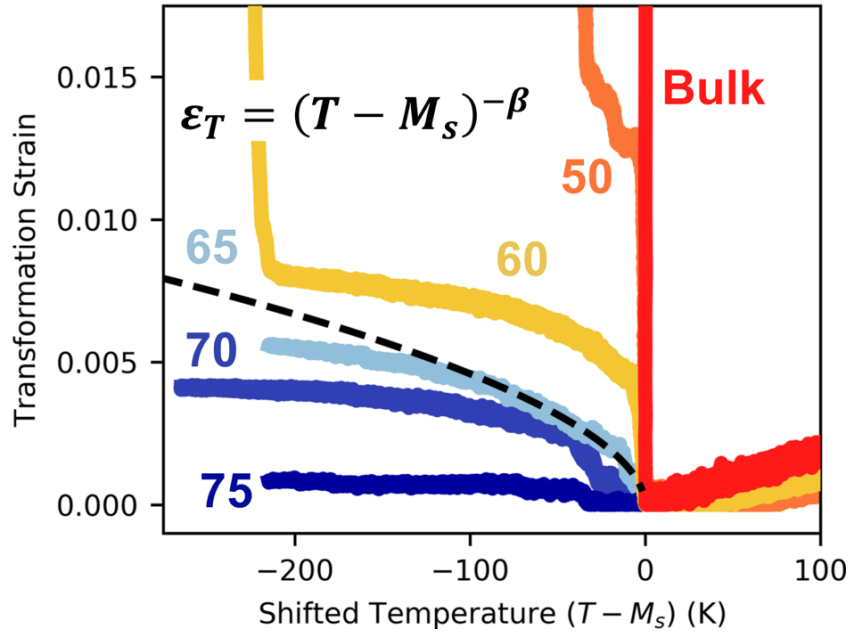


Fig. 2. Martensitic transformation strain order parameter. Bulk behavior contrasts the high NiAl volume fraction nanolaminates, all cooled to 25K. Fitting of scaling exponent shown for 65 at. % NiAl.

B. Domain structure exponent

An analysis of the atomic structure during the phase transition provides important additional insight regarding the nature of the phase transition. Figure 3 shows atomistic structures for the 65 at. % NiAl metamaterial below T_c . Atoms in the martensitic phase are colored in red and those in the austenite phase are transparent blue. The simulations reveal fascinating domain structure with interpenetrating phases and rough interfaces, completely uncharacteristic for martensitic transformations which exhibit planar domain walls with preferred lattice matching between the austenite and martensite: $[100]_A \parallel [110]_M$ in this system. In contrast, the domain structure in Fig. 3 is typical of second order transformations, where the difference between phases disappears leading to rough, jagged interfaces and a lack of a characteristic microstructural length. We note that the transformation only occurs within the $\text{Ni}_{63}\text{Al}_{37}$ region of the nanolaminate and that the structure shown in Fig. 3 is representative of observations for NiAl at. % between 60 and 75, beyond which the transformation is completely suppressed. Further, second order phase transformations are characterized by scaling in domain size distribution with power law exponent τ , often calculated for percolation. We performed a cluster analysis on the atoms in the martensitic phase to identify individual

domains, see details in Supplemental Fig. 3. We find the cluster size distribution indeed follows a power law from M_s until domains coalesce leading to one large martensitic phase, shown in Fig. 4. Supplemental Video 1 shows this cluster development throughout the cooling process, starkly contrasted by the bulk system in Supplemental Video 2. Finally, while the surface area and volume of 3D martensitic domains in first order transformations scale as $2/3$ ($A = V^{2/3}$), these martensite clusters in this second order transformation scale with an exponent of 0.86, or a fractal dimensionality of 2.58 (Supplemental Fig. 4). Resulting values of τ and fractal dimension are consistent across volume fraction until complete transformation suppression.

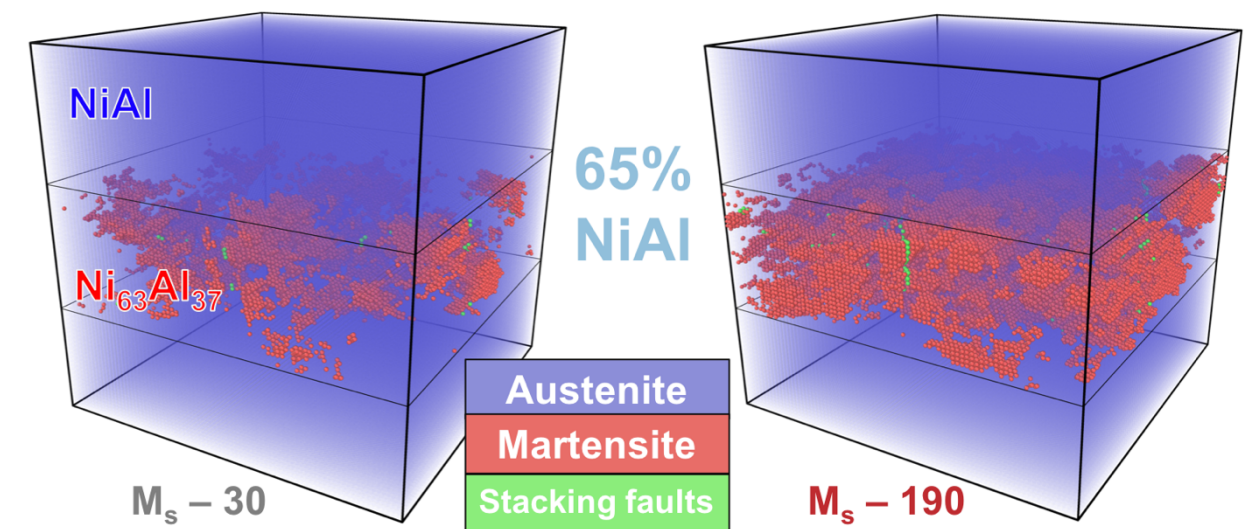


Fig. 3. Cluster fractal characteristics. Atomistic structure of the 65 at. % NiAl, exemplifying the localized, continuous nature of the martensitic transformation at two temperatures below M_s . Atoms classified as austenite are shown as transparent blue, martensite as red, and stacking faults as green.

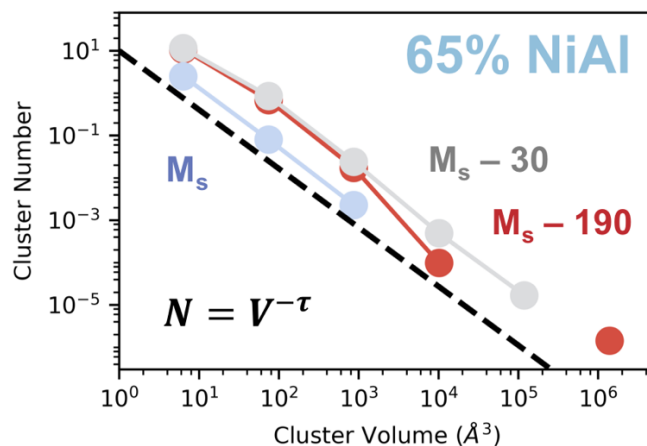


Fig. 4. Cluster scaling behavior. Cluster distribution showing scaling at M_s , extended scaling slightly below M_s , and one large, coalesced cluster far below M_s . Fitting of scaling exponent shown at M_s .

C. Exponent comparison

Having established the continuous nature and the expected scaling in domain size distribution, we now focus on how the related scaling laws and associated critical exponents compare with known systems that exhibit critical behavior, see Fig. 5. The values for β are comparable to several other critical phenomena, as demonstrated in Fig. 5A. The values for 65 at. % NiAl systems range from 0.45 and 0.55 and increase significantly for the highest NiAl fractions where the transformation is suppressed. The calculated values of τ for 65 at. % NiAl in Fig. 5B range from 1.3 to 1.5 are also comparable to similar transformations, experimental piezoelectric force microscopy in a relaxor ferroelectric[31], as well as spallation[32] and granular materials[18] from MD. In addition, the critical exponent γ governs the temperature dependence of the derivative of the order parameter with respect to applied field as the critical point is approached thermally. In our case, the gradient of transformation strain with respect to the applied strain field is computed using multiple values of the volume fraction of the second phase; fits are shown in Supplemental Fig. 5. The resulting value of γ , 0.85, calculated using all volume fractions from 60-75 at. % NiAl also corresponds reasonably well to existing critical behavior, Fig. 4C. The values near $\beta = 0.5$ and $\gamma = 1.0$ indicate this behavior fits within the mean-field universality class. Finally, characterization of the bulk system matching Fig. 2 and Fig. 3B highlights the disparate behavior of the first and second order systems (Supplemental Fig. 6).

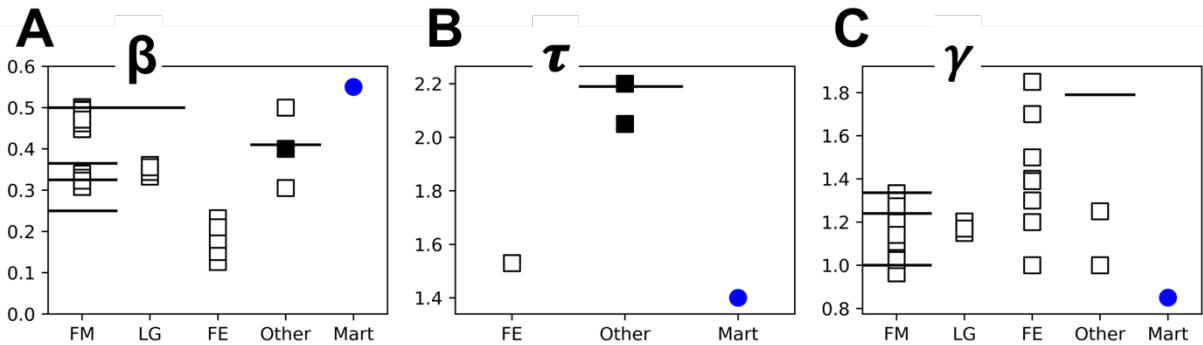


Fig. 5. Comparison of critical exponents. Data shown for (A) β , (B) τ , and (C) γ in the current martensitic study, with 65 at. % NiAl for β and τ , (Mart.) and well-known transformations: ferromagnetism (FM), liquid-gas coexistence (LG), ferroelectricity (FE), and other behavior. Lines represent theoretical results, open symbols experimental, and filled symbols MD. All values are described within Supplemental Tables 1-3.

In summary, we have shown that stress fields originating from a tailored second phase can change the nature of martensitic transformation in metallic alloys from first to second order. Importantly, our simulations show that the transformation can be described via scaling laws with exponent consistent with the mean-field universality class.

V. Discussion and outlook

Beyond the application of external fields discussed above, changes in the nature of the transformation have been demonstrated in ferroelectrics going from bulk to thin films [33] or via randomized composition [34], while martensitic transformations in metallic alloys are considered to be universally first order.

Interestingly, recent work has shown intriguing “higher order” characteristics in certain gum metals containing nanoscale variations in composition [19], [20], [35]. Ref. [19] showed both continuous stress-induced martensitic transformation due to mechanical confinement and a minimum in stiffness near the critical temperature. These observations are consistent with our theoretical findings: Fig. 2 shows continuous thermal transformation and Fig. 6 shows stiffness as a function of temperature for high volume fractions of NiAl strikingly similar to the aforementioned experimental results. Each sample used to evaluate stiffness was taken from the cooling simulations, equilibrated for 50 ps, and strained biaxially to 1% at a rate of $2 \cdot 10^8 \text{ s}^{-1}$ parallel to the laminate interface. A linear fit was taken from the resulting stress-strain data.

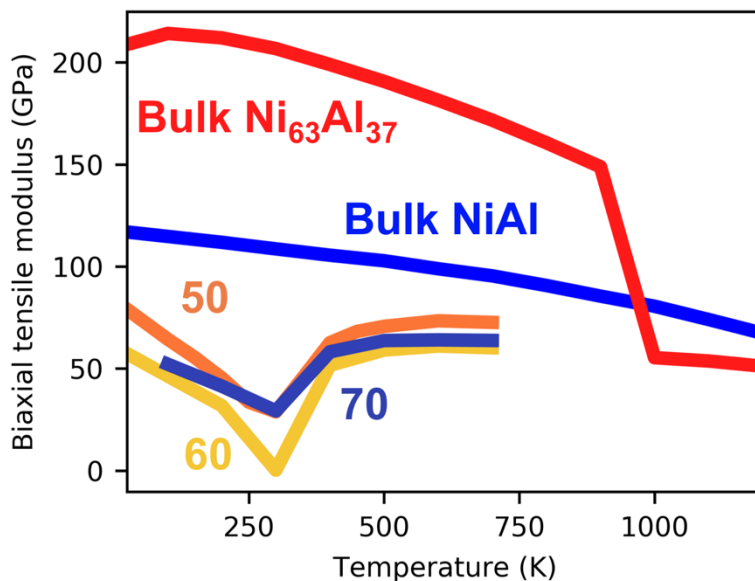


Figure 6: Stiffness in biaxial tension as a function of temperature for bulk phases and nanolaminates

Finally, we note that FELE has previously been used to create exciting new properties and functionalities in other systems; for example, ferroelectrics with negative capacitance [6], ultra-high piezoelectricity [11], and enhanced ferroelectricity through the related area of strain engineering [36], [37] have been demonstrated. The FELE approach described to transform a martensitic transition into a second order is rather general and could be applied to any alloy where an appropriate second phase can be identified. This could be used to develop new martensitic materials with ultra-low hysteresis for sensing and actuation applications. We anticipate that a coherent second phase could be incorporated via layered deposition (coherent metallic superlattices have been demonstrated using magnetron sputtering [38] and molecular beam epitaxy [39]) or by introducing coherent precipitates via traditional metallurgical processing [40].

Acknowledgements

This work was supported by the United States Department of Energy Basic Energy Sciences (DoE-BES) program under Program No. DE-FG02-07ER46399 (Program Manager John Vetrano). This work was performed in part under the auspices of the U.S. Department of Energy by Lawrence Livermore National

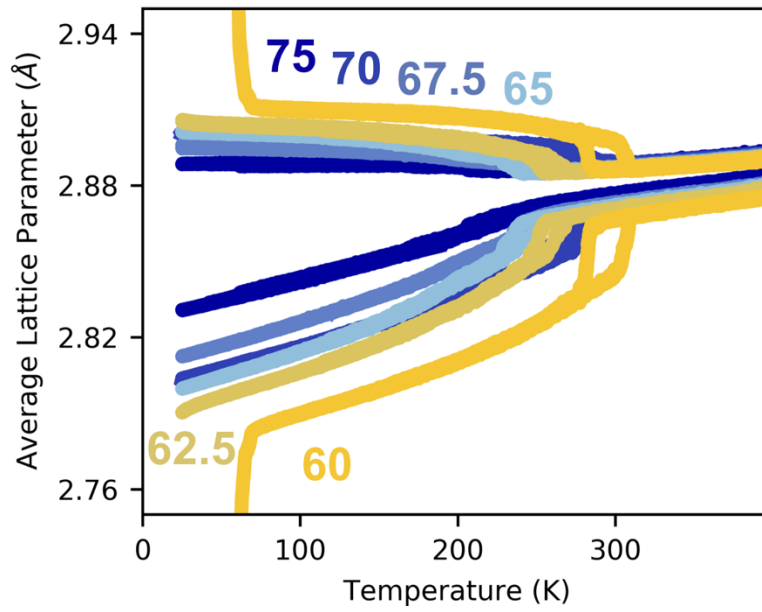
Laboratory under Contract DE-AC52-07NA27344. Computational resources from nanoHUB and Purdue University are gratefully acknowledged.

References

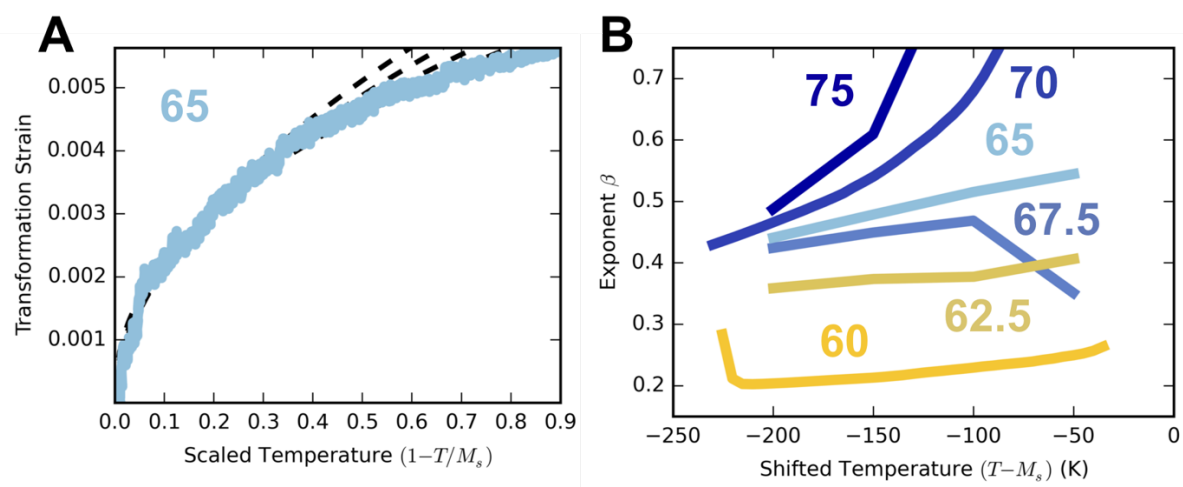
- [1] M. Ashby, “Materials—a brief history,” *Philos. Mag. Lett.*, vol. 88, no. 9–10, pp. 749–755, Sep. 2008.
- [2] A. Sharma, V. V. Tyagi, C. R. Chen, and D. Buddhi, “Review on thermal energy storage with phase change materials and applications,” *Renew. Sustain. Energy Rev.*, vol. 13, no. 2, pp. 318–345, Feb. 2009.
- [3] M. Wuttig and N. Yamada, “Phase-change materials for rewriteable data storage,” *Nat. Mater.*, vol. 6, no. 11, pp. 824–832, 2007.
- [4] K. M. Rabe, C. H. Ahn, and J.-M. Triscone, Eds., *Physics of ferroelectrics: a modern perspective*. Berlin ; New York: Springer, 2007.
- [5] J. F. Scott, “Applications of Modern Ferroelectrics,” *Science*, vol. 315, no. 5814, pp. 954–959, Feb. 2007.
- [6] A. Islam Khan, K. Chatterjee, B. Wang, S. Drapcho, L. You, C. Serrao, S. R. Bakaul, R. Ramesh, and S. Salahuddin, “Negative capacitance in a ferroelectric capacitor,” *Nat. Mater.*, vol. 14, no. 2, pp. 182–186, Feb. 2015.
- [7] K. Otsuka and X. Ren, “Physical metallurgy of Ti–Ni-based shape memory alloys,” *Prog. Mater. Sci.*, vol. 50, no. 5, pp. 511–678, Jul. 2005.
- [8] J. Zhao and Z. Jiang, “Thermomechanical processing of advanced high strength steels,” *Prog. Mater. Sci.*, vol. 94, pp. 174–242, May 2018.
- [9] M. E. Fisher, “The theory of equilibrium critical phenomena,” *Rep. Prog. Phys.*, vol. 30, no. 2, p. 615, 1967.
- [10] Z. Kutnjak, R. Blinc, and Y. Ishibashi, “Electric field induced critical points and polarization rotations in relaxor ferroelectrics,” *Phys. Rev. B*, vol. 76, no. 10, p. 104102, Sep. 2007.
- [11] F. Li, D. Lin, Z. Chen, Z. Cheng, J. Wang, C. Li, Z. Xu, Q. Huang, X. Liao, L.-Q. Chen, T. R. ShROUT, and S. Zhang, “Ultrahigh piezoelectricity in ferroelectric ceramics by design,” *Nat. Mater.*, vol. 17, no. 4, pp. 349–354, Apr. 2018.
- [12] Y. S. Oh, S. Artyukhin, J. J. Yang, V. Zapf, J. W. Kim, D. Vanderbilt, and S.-W. Cheong, “Non-hysteretic colossal magnetoelectricity in a collinear antiferromagnet,” *Nat. Commun.*, vol. 5, p. 3201, Jan. 2014.
- [13] M. Sanati, R. C. Albers, T. Lookman, and A. Saxena, “First-order versus second-order phase transformation in AuZn,” *Phys. Rev. B*, vol. 88, no. 2, p. 024110, Jul. 2013.
- [14] L. K. Nielsen, T. Bjørnholm, and O. G. Mouritsen, “Critical phenomena: Fluctuations caught in the act,” *Nature*, vol. 404, no. 6776, p. 352, Mar. 2000.
- [15] P. Limelette, A. Georges, D. Jérôme, P. Wzietek, P. Metcalf, and J. M. Honig, “Universality and Critical Behavior at the Mott Transition,” *Science*, vol. 302, no. 5642, pp. 89–92, Oct. 2003.
- [16] T. Bellini, L. Radzihovsky, J. Toner, and N. A. Clark, “Universality and Scaling in the Disordering of a Smectic Liquid Crystal,” *Science*, vol. 294, no. 5544, pp. 1074–1079, Nov. 2001.
- [17] X. Zeng, R. Kieffer, B. Glettner, C. Nurnberger, F. Liu, K. Pelz, M. Prehm, U. Baumeister, H. Hahn, H. Lang, G. A. Gehring, C. H. M. Weber, J. K. Hobbs, C. Tschierske, and G. Ungar, “Complex Multicolor Tilings and Critical Phenomena in Tetrachilic Liquid Crystals,” *Science*, vol. 331, no. 6022, pp. 1302–1306, Mar. 2011.
- [18] S. Ostojic, E. Somfai, and B. Nienhuis, “Scale invariance and universality of force networks in static granular matter,” *Nature*, vol. 439, no. 7078, pp. 828–830, Feb. 2006.
- [19] H. L. Wang, Y. L. Hao, S. Y. He, T. Li, J. M. Cairney, Y. D. Wang, Y. Wang, E. G. Obbard, F. Prima, K. Du, S. J. Li, and R. Yang, “Elastically confined martensitic transformation at the nano-scale in a multifunctional titanium alloy,” *Acta Mater.*, vol. 135, pp. 330–339, Aug. 2017.

- [20]Y. L. Hao, H. L. Wang, T. Li, J. M. Cairney, A. V. Ceguerra, Y. D. Wang, Y. Wang, D. Wang, E. G. Obbard, S. J. Li, and R. Yang, “Superelasticity and Tunable Thermal Expansion across a Wide Temperature Range,” *J. Mater. Sci. Technol.*, vol. 32, no. 8, pp. 705–709, Aug. 2016.
- [21]S. T. Reeve, A. Belessiotis-Richards, and A. Strachan, “Harnessing mechanical instabilities at the nanoscale to achieve ultra-low stiffness metals,” *Nat. Commun.*, vol. 8, no. 1, p. 1137, Dec. 2017.
- [22]K. Guda Vishnu and A. Strachan, “Shape memory metamaterials with tunable thermo-mechanical response via hetero-epitaxial integration: A molecular dynamics study,” *J. Appl. Phys.*, vol. 113, no. 10, p. 103503, Mar. 2013.
- [23]S. T. Reeve, K. Guda Vishnu, A. Belessiotis-Richards, and A. Strachan, “Tunability of martensitic behavior through coherent nanoprecipitates and other nanostructures,” *Acta Mater.*, 2018.
- [24]P. S. Khadkikar, I. E. Locci, K. Vedula, and G. M. Michal, “Transformation to Ni₅Al₃ in a 63.0 At. Pct Ni-Al alloy,” *Metall. Trans. A*, vol. 24, no. 1, pp. 83–94, Jan. 1993.
- [25]D. Farkas, B. Mutasa, C. Vailhe, and K. Ternes, “Interatomic potentials for B2 NiAl and martensitic phases,” *Model. Simul. Mater. Sci. Eng.*, vol. 3, no. 2, pp. 201–214, Mar. 1995.
- [26]K. R. Morrison, M. Cherukara, K. Guda Vishnu, and A. Strachan, “Role of atomic variability and mechanical constraints on the martensitic phase transformation of a model disordered shape memory alloy via molecular dynamics,” *Acta Mater.*, vol. 69, no. 110, pp. 30–36, May 2014.
- [27]K. R. Morrison, M. Cherukara, H. Kim, and A. Strachan, “Role of grain size on the martensitic transformation and ultra-fast superelasticity in shape memory alloys,” *Acta Mater.*, vol. 95, pp. 37–43, 2015.
- [28]S. Plimpton, “Fast Parallel Algorithms for Short-Range Molecular Dynamics,” *J. Comput. Phys.*, vol. 117, no. 1, pp. 1–19, Mar. 1995.
- [29]A. Stukowski, “Visualization and analysis of atomistic simulation data with OVITO—the Open Visualization Tool,” *Model. Simul. Mater. Sci. Eng.*, vol. 18, no. 1, p. 015012, Jan. 2010.
- [30]P. M. Larsen, S. Schmidt, and J. Schiøtz, “Robust structural identification via polyhedral template matching,” *Model. Simul. Mater. Sci. Eng.*, vol. 24, no. 5, p. 055007, Jun. 2016.
- [31]W. Kleemann, J. Dec, P. Lehnen, R. Blinc, B. Zalar, and R. Pankrath, “Uniaxial relaxor ferroelectrics: The ferroic random-field Ising model materialized at last,” *EPL Europhys. Lett.*, vol. 57, no. 1, p. 14, Jan. 2002.
- [32]A. Strachan, T. Çağın, and W. A. Goddard, “Critical behavior in spallation failure of metals,” *Phys. Rev. B*, vol. 63, no. 6, p. 060103, Jan. 2001.
- [33]A. V. Bune, V. M. Fridkin, S. Ducharme, L. M. Blinov, S. P. Palto, A. V. Sorokin, S. G. Yudin, and A. Zlatkin, “Two-dimensional ferroelectric films,” *Nature*, vol. 391, no. 6670, pp. 874–877, Feb. 1998.
- [34]V. V. Lemanov, E. P. Smirnova, P. P. Syrnikov, and E. A. Tarakanov, “Phase transitions and glasslike behavior in Sr(1-x)Ba(x)TiO₃,” *Phys. Rev. B*, vol. 54, no. 5, pp. 3151–3157, Aug. 1996.
- [35]J. Zhu, Y. Gao, D. Wang, T.-Y. Zhang, and Y. Wang, “Taming martensitic transformation via concentration modulation at nanoscale,” *Acta Mater.*, vol. 130, pp. 196–207, May 2017.
- [36]J. H. Haeni, P. Irvin, W. Chang, R. Uecker, P. Reiche, Y. L. Li, S. Choudhury, W. Tian, M. E. Hawley, B. Craigo, A. K. Tagantsev, X. Q. Pan, S. K. Streiffer, L. Q. Chen, S. W. Kirchoefer, J. Levy, and D. G. Schlom, “Room-temperature ferroelectricity in strained SrTiO₃,” *Nature*, vol. 430, no. 7001, pp. 758–761, Aug. 2004.
- [37]K. J. Choi, M. Biegalski, Y. L. Li, A. Sharan, J. Schubert, R. Uecker, P. Reiche, Y. B. Chen, X. Q. Pan, V. Gopalan, L.-Q. Chen, D. G. Schlom, and C. B. Eom, “Enhancement of Ferroelectricity in Strained BaTiO₃ Thin Films,” *Science*, vol. 306, no. 5698, pp. 1005–1009, Nov. 2004.
- [38]Q. M. Wei, X.-Y. Liu, and A. Misra, “Observation of continuous and reversible bcc–fcc phase transformation in Ag/V multilayers,” *Appl. Phys. Lett.*, vol. 98, no. 11, p. 111907, Mar. 2011.
- [39]S. Park, X. Zhang, A. Misra, J. D. Thompson, M. R. Fitzsimmons, S. Lee, and C. M. Falco, “Tunable magnetic anisotropy of ultrathin Co layers,” *Appl Phys Lett*, vol. 86, no. 4, pp. 2–4, 2005.

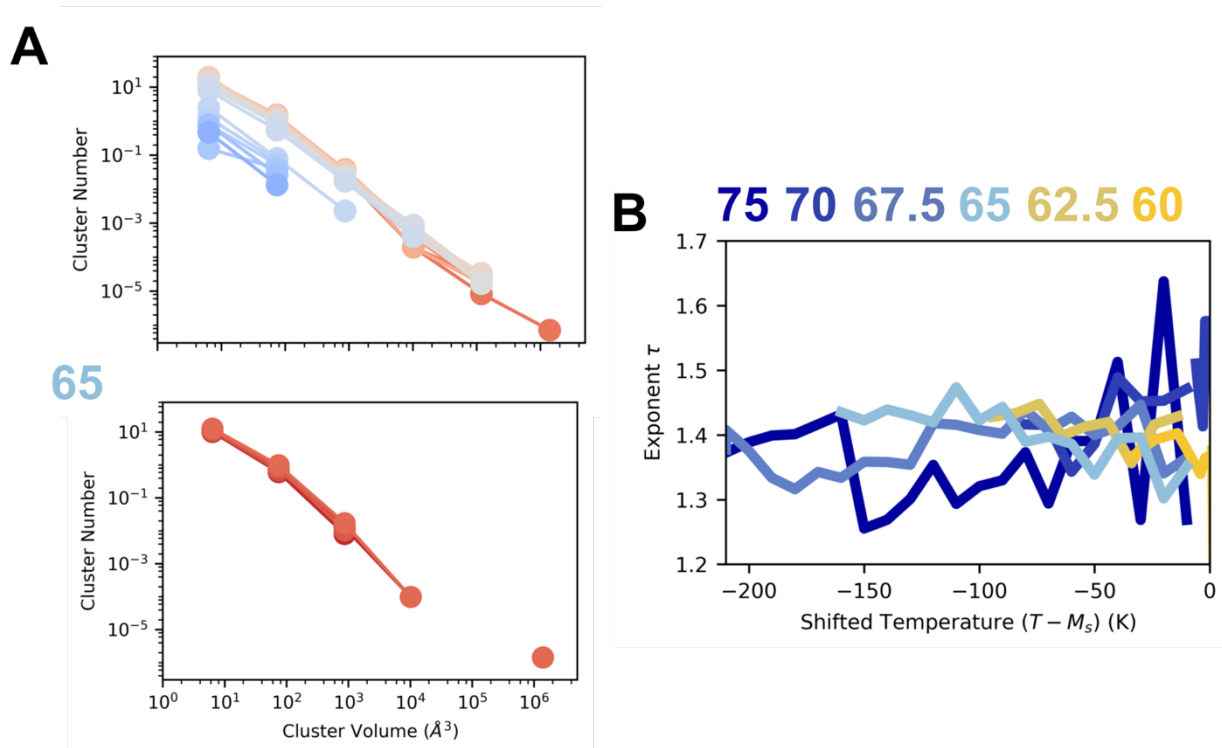
- [40]J. Khalil-Allafi, A. Dlouhy, and G. Eggeler, “Ni₄Ti₃-precipitation during aging of NiTi shape memory alloys and its influence on martensitic phase transformations,” *Acta Mater.*, vol. 50, no. 17, pp. 4255–4274, Oct. 2002.
- [41]B. Yu, W. Sun, J. Fan, X. Lan, W. Zhang, Y. Zhu, H. Han, L. Zhang, L. Ling, and H. Yang, “Scaling study of magnetic phase transition and critical behavior in Nd_{0.55}Sr_{0.45}Mn_{0.98}Ga_{0.02}O₃ manganite,” *Mater. Res. Bull.*, vol. 99, pp. 393–397, Mar. 2018.
- [42]K. Dadda, S. Alleg, S. Souilah, J. J. Suñol, E. Dhahri, L. Bessais, and E. K. Hlil, “Critical behavior, magnetic and magnetocaloric properties of melt-spun Ni₅₀Mn₃₅Sn₁₅ ribbons,” *J. Alloys Compd.*, vol. 735, pp. 1662–1672, Feb. 2018.
- [43]D. Stauffer and A. Aharony, *Introduction To Percolation Theory*, 2 edition. London: Taylor & Francis, 1994.



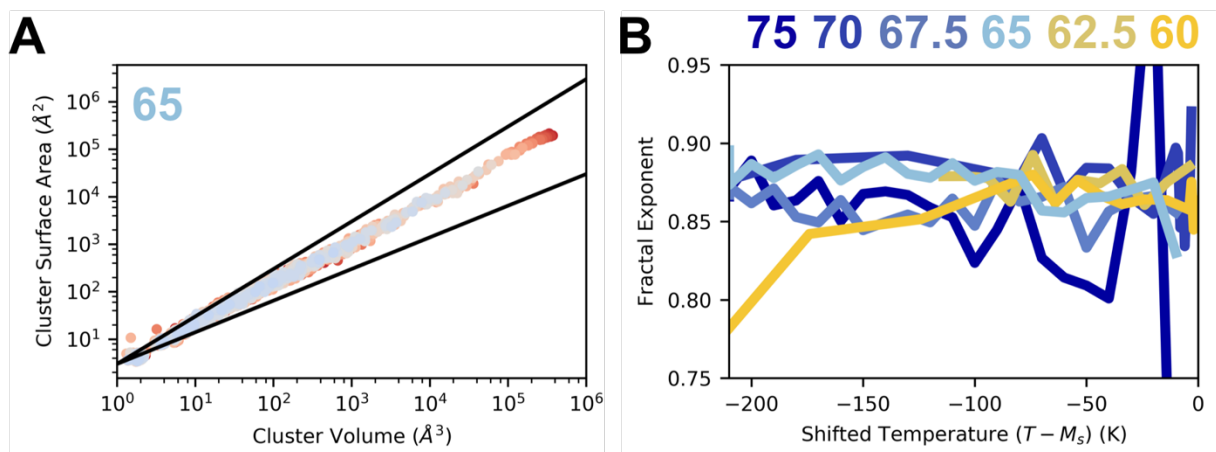
Supplemental Figure 1: Cooling and heating cycle for all systems above 60 at. % NiAl. Note the lack of hysteresis for all nanolaminates other than 60 at. % NiAl.



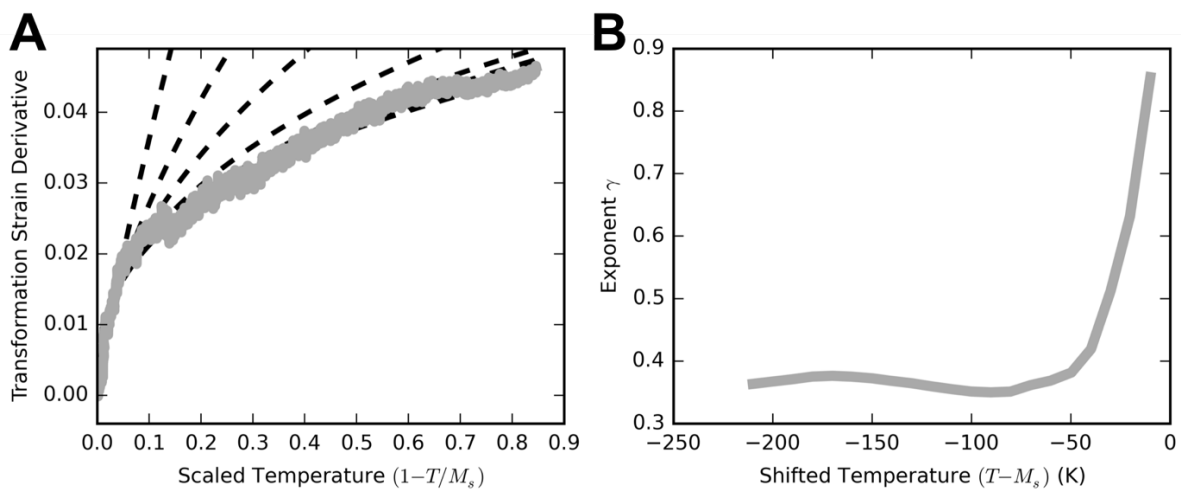
Supplemental Figure 2: Calculation of exponent β . (A) fitting example for 65 at. % NiAl and (B) exponents as a function of temperature.



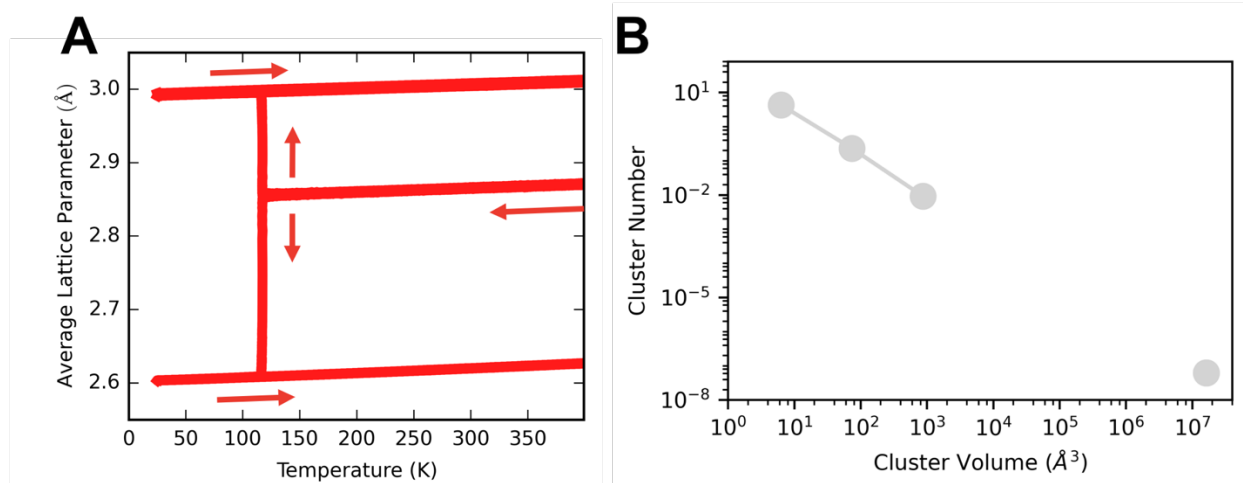
Supplemental Figure 3: Calculation of exponent τ . (A) cluster distribution at and below M_s for 65 at. % NiAl (upper) and far below M_s for 65 at. % NiAl (lower) and (B) exponents as a function of temperature below the transition.



Supplemental Figure 4: Calculation of fractal exponent. (A) fitting example for 65 at. % NiAl, with guides of slope 1 and 2/3 (bulk), and (B) exponents as a function of temperature.



Supplemental Figure 5: Calculation of exponent γ . (A) fitting and (B) exponent as a function of temperature.



Supplemental Figure 6: Bulk $\text{Ni}_{63}\text{Al}_{37}$ characteristics. (A) cooling and heating cycle and (B) cluster distribution at M_s with near complete transformation.

Supplemental Table 1: Beta critical exponents from literature

Behavior	Material/Theory	Exponent	Reference
Ferromagnetic (FM)	Mean field	0.5	[9]
	3D Heisenberg	0.365	
	3D Ising	0.325	
	Tri-critical mean field	0.25	
	Iron	0.34	
	Nickel	0.33	
	$\text{Nd}_{0.5}\text{Sr}_{0.5}\text{MnO}_3$	0.323	[41]
	$\text{Pr}_{0.5}\text{Sr}_{0.5}\text{MnO}_3$	0.448	[42]
	$\text{Ni}_{50}\text{Mn}_{35}\text{Sn}_{15}$	0.501	
Liquid-Gas Coexistence (LG)	van der Waals	0.5	[9]
	CO_2	0.333	
	Xe	0.345	
	He	0.361	
Ferroelectric (FE)	$\text{Sr}_{0.61-x}\text{Ce}_x\text{Ba}_{0.39}\text{Nb}_2\text{O}_6$	0.14	[31]
Order-Disorder	CuZn	0.305	[9]
Mott	$(\text{Cr}_{0.989}\text{V}_{0.011})_2\text{O}_3$	0.5	[15]
Spallation	Ta (MD)	0.4	[32]
Percolation	3D	0.41	[43]

Supplemental Table 2: Tau critical exponents from literature

Behavior	Material/Theory	Exponent	Reference
Ferroelectric (FE)	$\text{Sr}_{0.61-x}\text{Ce}_x\text{Ba}_{0.39}\text{Nb}_2\text{O}_6$ (2D measurement)	1.53	[31]
Spallation	Ta (MD)	2.2	[32]
Granular material	(MD)	2.06	[18]
Percolation	3D	2.18	[43]

Supplemental Table 3: Gamma critical exponents from literature

Behavior	Material/Theory	Exponent	Reference
Ferromagnetic (FM)	Mean field	1.0	[9]
	3D Heisenberg	1.336	
	3D Ising	1.24	
	Tri-critical mean field	1.0	
	Iron	1.333	
	Nickel	1.32	
	$\text{Nd}_{0.5}\text{Sr}_{0.5}\text{MnO}_3$	1.201	[41]
	$\text{Pr}_{0.5}\text{Sr}_{0.5}\text{MnO}_3$	1.334	[42]
	$\text{Ni}_{50}\text{Mn}_{35}\text{Sn}_{15}$	0.963	
Liquid-Gas Coexistence (LG)	van der Waals	1.0	[9]
	CO_2	1.20	
	Xe	1.203	
	He	1.15	
Ferroelectric (FE)	$\text{Sr}_{0.61-x}\text{Ce}_x\text{Ba}_{0.39}\text{Nb}_2\text{O}_6$	1.0	[31]
Order-Disorder	CuZn	1.25	[9]
Mott	$(\text{Cr}_{0.989}\text{V}_{0.011})_2\text{O}_3$	1.0	[15]
Percolation	3D	1.80	[43]